Author Manuscript

Analysis of deep complex-valued convolutional neural networks for MRI reconstruction and phase-focused applications

Elizabeth Cole[1], **Joseph Cheng**[1], **John Pauly**[1], **Shreyas Vasanawala**[2]

[1]Department of Electrical Engineering, Stanford University, Stanford, CA, USA

[2]Department of Radiology, Stanford University, Stanford, CA, USA

Abstract

Purpose: Deep learning has had success with MRI reconstruction, but previously published works use real-valued networks. The few works which have tried complex-valued networks have not fully assessed their impact on phase. Therefore, the purpose of this work is to fully investigate end-to-end complex-valued convolutional neural networks (CNNs) for accelerated MRI reconstruction and in several phase-based applications in comparison to 2-channel real-valued networks.

Methods: Several complex-valued activation functions for MRI reconstruction were implemented, and their performance was compared. Complex-valued convolution was implemented and tested on an unrolled network architecture and a U-Net–based architecture over a wide range of network widths and depths with knee, body, and phase-contrast datasets.

Results: Quantitative and qualitative results demonstrated that complex-valued CNNs with complex-valued convolutions provided superior reconstructions compared to real-valued convolutions with the same number of trainable parameters for both an unrolled network architecture and a U-Net–based architecture, and for 3 different datasets. Complex-valued CNNs consistently had superior normalized RMS error, structural similarity index, and peak SNR compared to real-valued CNNs.

Conclusion: Complex-valued CNNs can enable superior accelerated MRI reconstruction and phase-based applications such as fat–water separation, and flow quantification compared to real-valued convolutional neural networks.

Keywords

complex-valued models; convolutional neural networks; image reconstruction; learning representations; MRI

Correspondence: Elizabeth Cole, Department of Electrical Engineering, Stanford University, Packard Electrical Engineering, Room 306, 350 Serra Mall, Stanford, CA 94305, ekcole@stanford.edu.

CONFLICT OF INTEREST

Shreyas Vasanawala is a founder of Arterys. Joseph Cheng currently works at Apple, Inc. John Pauly is on the board of Heartvista.

SUPPORTING INFORMATION

Additional Supporting Information may be found online in the Supporting Information section.

1 | INTRODUCTION

MRI is a useful medical imaging technique that, unlike CT, does not use harmful ionizing radiation. However, MRI is relatively slow. A typical scan requires patients to remain still for a long period of time to produce images of diagnostic quality. Scan times can be significantly reduced by undersampling k-space in various sampling patterns with negligible image quality loss.

Traditionally, reconstructing images from these accelerated scans has involved leveraging techniques such as parallel imaging[1,2] and compressed sensing (CS).[3] More recently, convolutional neural networks (CNNs) have been shown to provide a rapid and robust solution to MRI reconstruction as an alternative to slow iterative solvers. These reconstruction networks span a vast range of architectures and techniques. Examples include cascaded networks,[4] generative adversarial networks,[5,6] unrolled methods,[7–11] hybrid networks,[12–14] U-Nets,[15–17] and automated transform by manifold approximation.[18]

Even though MRI data are complex-valued, the vast majority of current deep learning (DL) frameworks do not support complex-valued DL. Complex representations have not traditionally appeared in many DL architectures because most standard computer vision datasets are real-valued. In MRI, signals collected are complex-valued with both a real and imaginary component. Most reconstruction networks split real and imaginary components into 2 separate real-valued channels,[5,8,10–13,18–20] which may not be the best way to represent complex numbers in a neural network. Recent work has shown the representative power and accuracy of complex-valued deep neural networks,[21] which motivates applying complex-valued CNNs to MRI reconstruction.

Using complex numbers enables accurately representing both magnitude and phase, which are 2 essential components of certain signals. Phase is valuable in many MRI applications, including blood flow, QSM, fat–water separation, and chemical shift imaging. Thus, constructing a network that more accurately reconstructs the phase may improve various MRI applications.

A few DL networks applied to MRI reconstruction[22–25] have demonstrated that DL performance can be improved over real-valued networks using complex-valued networks. In MRI reconstruction, Dedmari et al[22] applied a complex dense fully convolutional network to MRI reconstruction using complex convolution and complex batch normalization. The authors demonstrated improved recovery of anatomy and perceptual quality using a complex-valued network in comparison to a real-valued network. Wang et al[23,24] applied complex-valued convolution to a cascaded network for parallel MRI reconstruction. The authors used a complex-valued network and chose a residual structure to avoid vanishing gradient problems and to improve network convergence.

However, these works reconstruction primarily evaluated the quality of magnitude reconstructions and minimally treated how complex networks affect phase reconstruction and other phase-related applications. Additionally, these works only tested a single complex-valued activation function for reconstruction, whereas testing several different complex-valued activation functions could have added value to the comparisons. None of these works

experimented with an unrolled network architecture,[7] which is a model-driven approach that incorporates known MR physics. Unrolled networks have demonstrated powerful results in MRI reconstruction. [,7,8,10,26–28–] Therefore, it is important to understand how complex-valued processing performs on an unrolled network architecture. Finally, previous works do not evaluate whether complex-valued networks perform better than real-valued networks over a variety of datasets, network architectures, and network size.

In this work, we investigate potential improvement in recovery of image phase using complex-valued CNNs compared to real-valued CNNs. We present an extensive study, examining several datasets, network architectures, and network sizes. We experiment with complex-valued convolution and complex-valued activation functions. We investigate performance of real-valued and complex-valued CNNs on phase reconstruction. Therefore, we compare results of complex versus real models on fat–water separation and flow quantification, tasks that heavily rely on accurate phase reconstruction, which is a novel contribution to studying complex models for MRI. In our comparisons, we give attention to both phase and magnitude reconstructions using image metrics, which take both phase and magnitude into account, as well as showing both phase and magnitude representative images.

Our novel contributions in this paper are:

1. Quantitative and qualitative comparison of reconstructions from real versus complex networks for an unrolled network architecture across an extensive range of width and depth, presented in Results section B and Results section C.

2. Quantitative and qualitative comparison of reconstructions from real versus complex networks for a U-Net–based architecture, presented in Results section D.

3. A novel comparison of real versus complex model performance on tasks, which heavily rely on accurate phase reconstruction: fat–water separation and flow quantification, presented in Results section F and H.

4. A formulation of complex-valued processing for MRI reconstruction, including complex convolution and complex activation functions, made publicly available at: https://github.com/MRSRL/complex-networks-release

2 | METHODS

2.1 | Complex-valued convolution

We begin with our representation of complex numbers within our convolutional neural network. A complex number can be represented by $d = a + ib$, where $a = \text{Re}\{d\}$ and $b = \text{Im}\{d\}$ are the respective real and imaginary components.

Instead of separating real and imaginary components of our data and performing real-valued convolution, we performed the complex-valued equivalent. To do so, we convolved a complex filter matrix $W = X + iY$, where X and Y are real-valued filters, with our complex

data $d = a + ib$. Using the distributive property of convolution, we can split this convolution into 4 separate real-valued convolutions:

$$W * d = (X + iY) * (a + ib) = (X * a - Y * b) + i(Y * a + X * b). \tag{1}$$

These convolutions can be represented in matrix form by:

$$\begin{bmatrix} Re(W * d) \\ Im(W * d) \end{bmatrix} = \begin{bmatrix} X & -Y \\ Y & X \end{bmatrix} * \begin{bmatrix} a \\ b \end{bmatrix} \cdot \begin{bmatrix} Re(W * d) \\ Im(W * d) \end{bmatrix} = \begin{bmatrix} X & -Y \\ Y & X \end{bmatrix} * \begin{bmatrix} a \\ b \end{bmatrix}. \tag{2}$$

A complex-valued convolutional layer has half as many parameters compared to its real-valued counterpart. To understand this, refer to Supplementary Information Methods section A.

For a fair comparison between complex-valued and real-valued models, we set the number of feature maps so each model has the same number of parameters.

2.2 | Complex-valued activation functions

Numerous activation functions have been proposed to work with complex numbers. In a standard real-valued CNN, we use the rectified linear unit (ReLU) applied separately to the 2 channels. We experiment with modReLU,[21,29] CReLU,[21] zReLU,[21] and the cardioid function.[30] The motivation behind these activation functions can be found in Supporting Information Methods section B.

The ReLU function is defined as:

$$\mathrm{Re}LU(d) = \begin{cases} d & \text{if } d \geq 0 \\ 0 & \text{otherwise} \end{cases}. \tag{3}$$

The ReLU function is defined as:

$$mod\,Re\,LU(d) = Re\,LU(\left| d \right| + b)e^{i\theta_d}, \tag{4}$$

where $d \in \mathbb{C}$; b is a learnable real-valued bias parameter; and θ_d is the phase of d.

The $\mathbb{C}$ReLU function, which applies separate ReLUs on real and imaginary components of a complex-valued input and adds them, is defined as:

$$\mathbb{C}\mathrm{ReLU}(d) = Re\,LU(\mathrm{Re}\{d\} + i\mathrm{Re}LU(Im\{d\}). \tag{5}$$

The zReLU function is defined as:

$$z\mathrm{Re}LU(d) = \begin{cases} d, & if\ \theta_d \in [0, \frac{\pi}{2}] \\ 0, & \text{otherwise} \end{cases}. \tag{6}$$

The cardioid function, which scales the input magnitude but retains the input phase, is defined as:

$$\text{cardioid}(d) = \frac{1}{2}d(1 + \cos\theta_d). \qquad (7)$$

2.3 | Network architecture and training

MRI reconstruction with CNNs has been demonstrated with a variety of network architectures. We chose to use 2 different reconstruction networks to compare performance of real and complex convolution in order to demonstrate complex-valued processing across different architectures. The first network used is based on an unrolled optimization with deep priors based on the iterative soft-shrinkage algorithm.[7,31] Unrolled networks have been commonly used in state-of-the-art MRI reconstruction [7,8,10,26,27,32] due to good performance and having the advantage of reducing the reconstruction solution space, which refers to the set of possible reconstructions that the model can be trained to produce. The unrolled network architecture is shown in Figure 1A. This network repeats 2 different blocks: a data consistency block and a de-noising block.

The first block of Figure 1A, known as the update block, is used to enforce consistency with the measured data samples. This block, otherwise known as the data consistency block, makes sure the final reconstructed image is consistent with the measured data to minimize the chance of hallucination. More information on this can be found in the Supplementary Information Methods section B. The second block of Figure 1A is used to denoise the image. The second network used is based on U-Net.[6,16,17] U-Net was chosen as another architecture because U-Net is a quite different architecture compared to variants of the iterative soft-shrinkage algorithm-based unrolled architecture, such as variational[10] and model-based DL[33] networks. U-Net is also of increasing interest in MRI reconstruction. [6,16,17,34–37] The U-Net-based architecture is shown in Figure 1B.

The networks were trained with an L_1 loss. The networks were optimized with the Adam optimizer[38] with $\beta_1 = 0.9$, $\beta_2 = 0.999$ and a learning rate of 0.001. The U-Net was trained with a batch size of 3, and the unrolled network was trained with a batch size of 2. Networks were trained using an NVIDIA Titan Xp graphics card and an NVIDIA GeForce GTX 1080 Ti graphics card. For further information, refer to Supporting Information Methods section B. The proposed methods were implemented in Python 2.7 using Tensorflow 1.14. To compute image quality, we evaluated normalized RMS error (NRMSE), peak SNR (PSNR), and structural similarity index (SSIM)[39] between the reconstructed image and the fully sampled ground truth. NRMSE error and PSNR are evaluated on complex-valued images; however, SSIM is evaluated on magnitude-only images. An explanation of this is in Supporting Information section B.

2.4 | Dataset details

Three sets of data were obtained with Institutional Review Board approval and subject-informed consent. First, fully sampled knee images were acquired using 8 coil arrays and a 3D fast spin echo sequence with proton density weighting with fat saturation,[40] which we expected to have the least phase variation. Fifteen subjects were used for training, and 3 subjects were used for testing. The readout was in the superoinferior direction; thus, the

axial direction was subsampled. Each subject had a complex-valued volume of size $320 \times 320 \times 256$ that was split into axial slices of size $320 \times V256$. The knee dataset is available online: http://old.mridata.org/fullysampled/knees.

The second dataset that we used contained body scans, which were acquired using 16 coil arrays and a 3D RF-spoiled dual gradient-echo spoiled gradient-recalled sequence with gadolinium contrast.[41,42] Here, we expected greater phase variation. Phase should systematically vary between the 2 echoes depending on tissue composition. This dataset could be used for fat–water separation, for which phase is important information. On average, TE_1 was 1.1 ms and TE_2 was 2.2 ms. The fully sampled direction was left–right. The dataset was split into 2D coronal slices of 104 patients for training and 45 patients for testing. Each subject had a complex-valued volume of size $224 \times 220 \times 180$ that was split into coronal slices of size 220×180, with each slice considered a separate training example.

Third, fully sampled 2D phase-contrast (2D PC) cine images were acquired using 8 coil arrays in 180 pediatric patients. Signal phase directly encoded blood velocity, which was the clinical goal of the acquisition. Through-plane velocity was encoded for various vessels of interest including the aorta, pulmonary artery/vein, mesenteric vein, and splenic vein. Data acquisition was performed across several 1.5 Tesla and 3.0 Tesla scanners (Discovery MR 750, GE Healthcare; Waukesha, WI), with a flip angle of 20 degrees, a complex-valued volume of approximate size $192 \times 256 \times 18$, temporal resolution of 5.056 ms, and V_{enc} ranging between 80 and 500 cm/s. 124 subjects were used for training, and 44 subjects were used for testing. Each cine dataset was split up by cardiac frames and slices because the network architecture accommodated 2D data.

Further sequence details are in Supporting Information Table S1. For each dataset, variable-density sampling masks were generated using pseudo-random Poisson-disc sampling on the Cartesian grid, with acceleration factors ranging from 2 to 9 with a fully sampled calibration region of 20×20 in the center of k-space. Many sampling masks were used in order to train the model for a general Poisson-disc pattern, not just one sampling pattern. Sensitivity maps for the data acquisition model were estimated from k-space data in the calibration region using ESPIRiT.[43] The Berkeley Advanced Reconstruction Toolbox[44] was used to estimate sensitivity maps, generate Poisson-disc sampling masks, and perform a CS^3 reconstruction with L_1-wavelet regularization of these datasets for comparison purposes.

2.5 | Experiments

In the following experiments, we evaluated the effect of number of feature maps, network depth, and network architecture on reconstruction using complex-valued and real-valued networks. We did an extensive search of network parameters for later experiments, which is an extension of previous work. We then evaluated the performance in flow quantification and fat–water separation of complex-valued and real-valued networks.

To encourage reproducible research, we provide a software package in Tensorflow 1.14 to reproduce the results described in this article, which can be downloaded from: https://github.com/MRSRL/complex-networks-release.

2.5.1 | Experiment 1: Activation functions

The unrolled network was trained and tested on the knee dataset using real convolution and complex convolution. When real convolution was used, ReLU was applied separately to the real and imaginary channels. When complex convolution was used, the network was additionally trained and tested using the activation functions introduced above: modReLU, CReLU, zReLU, and the cardioid function. The goal of this experiment was to compare the reconstruction performance of real and complex convolution as well as the reconstruction performance of different complex-valued activation functions. The impact of various proposed complex-valued activation functions on reconstruction accuracy was assessed by calculating average PSNR, NRMSE, and SSIM on a test dataset. The number of iterations and feature maps were fixed for this experiment to 4 and 256, respectively. The real-valued and complex-valued networks were designed to have nearly identical numbers of parameters. For all future experiments, we used CReLU as the complex-valued activation function because it performed the best over the other activation functions.

2.5.2 | Experiment 2: Complex convolution and network width

Using the knee dataset, we evaluated the impact of the width of the unrolled network on the performance of the real versus complex model by fixing the number of iterations to 4 while varying the number of feature maps in each layer. We defined network width as the number of feature maps per layer. To match the number of parameters for both models while keeping the number of unrolled iterations the same, the real-valued model had 6, 12, 22, 46, 90, and 182 feature maps, whereas the complex-valued model had 8, 16, 32, 64, 128, and 256 feature maps. We trained and tested the unrolled network using real and complex convolution over a wide range of network widths because we wanted to see if the performance of the complex-valued model was consistent over a range of number of feature maps. We did this by training many models of different sizes. We also wanted to investigate whether the performance of the real-valued and complex-valued models converged as both models gained more representational capacity.[45] We measured performance by calculating PSNR, NRMSE, and SSIM.

2.5.3 | Experiment 3: Complex convolution and network depth

We investigated if the difference in performance of the real-valued and complex-valued models would converge faster as the number of parameters in each model increased. We defined network depth as the number of unrolled iterations per layer. Using the knee dataset, we varied the depth of the unrolled network by training real and complex-valued networks with 2, 4, 8, and 12 iterations in each layer. The goal of this experiment was to see if the difference in performance, measured through the image metrics PSNR, NRMSE, and SSIM, of the real-valued and complex-valued models converged as the number of parameters in each model increased.

2.5.4 | Experiment 4: U-Net performance

We then trained and evaluated the reconstruction performance of 2 models, 1 with real convolution, and 1 with complex convolution, using the U-Net architecture. Our goal was to compare real and complex convolution on an additional architecture to investigate whether the difference in performance of the models remained over a variety of network architectures.

2.5.5 | Experiment 5: Dual gradient-echo dataset—From the results of experiments 1-4, we decided to hereafter use an unrolled network with 128 feature maps and 4 iterations to strike a balance between performance and memory usage. With a good candidate network, we performed 4 experiments with clinically important applications that depend on phase.

We then trained and evaluated the unrolled network on the dual gradient-echo dataset for 2 models, 1 with real convolution and 1 with complex convolution. The goal of this experiment was to investigate whether the difference in performance of models with real and complex convolution was consistent in a dataset with more phase variation. The dual-echo dataset had more phase information than the knee dataset. Therefore, this experiment was specifically meant to measure effects of complex-valued convolution on phase.

2.5.6 | Experiment 6: Fat–water separation—We implemented the fat–water separation algorithm described in Berglund et al[46] and applied it to the dual-echo dataset to compare the complex or real models of experiment 5 for fat–water separation. This is a clinically important application that relies on phase. Fat–water separation is important for applications such as liver fat quantification or T_1 separation. Obtaining fat-suppressed images is used for post-contrast T_1-weighted imaging in the body and extremities. This is commonly obtained by dual-echo imaging, which offers a balance between obtaining fat–water separation and scan time. Whereas separation from 3 echoes is more robust, the time penalty is significant.

2.5.7 | Experiment 7: Phase-contrast dataset—We also trained and evaluated the unrolled network on the 2D PC cine dataset for 2 models, 1 with real convolution and 1 with complex convolution. The 2D PC cine dataset had more phase information than both the knee and the dual-echo dataset. Phase-contrast data are used for velocity-encoded images. Therefore, it was important to accurately reconstruct the phase information of such 2D PC data. The reconstruction of 2D PC images is important for extensive evaluation of patients with heart disease.

2.5.8 | Experiment 8: Flow quantification—To further analyze the accuracy of phase reconstruction in a clinical application, we compared the real and complex models' performance on flow quantification of the 2D PC cine dataset. Accurate flow quantification is important for measuring patients' blood flow in the arteries and the heart. Flow quantification is a much more clinically relevant metric than conventional image metrics. Also, image metrics are calculated over the entire image, whereas flow quantification is calculated only over the region of interest. For each exam, we selected a region of interest and measured the average flow (L/min) and the peak velocity (cm/s) of the real and complex models' reconstructions. These flow metrics were measured using Arterys (Arterys Inc, San Francisco, CA), a medical image analysis tool. We then compared these flow statistics to the ground truth and evaluated which model had more accurate flow.

3 | RESULTS

3.1 | Experiment 1: Activation functions

Comparisons of the various complex-valued activation functions' reconstruction accuracy in the unrolled network on the knee dataset are shown in Table 1. ℂReLU achieves the best performance overall, with zReLU almost achieving the same performance.

In the unrolled network that was trained and tested on the knee dataset, the complex-valued CNN achieved superior PSNR (36.08 ± 3.06) compared to the real-valued CNN (34.18 ± 4.51). The complex-valued CNN achieved superior NRMSE (0.13 ± 0.04) compared to the real-valued CNN (0.16 ± 0.06). Finally, the complex-valued CNN achieved superior SSIM (0.92 ± 0.02) compared to the real-valued CNN (0.90 ± 0.07).

Representative magnitude images from the unrolled models for the spin-echo–based knee dataset are displayed in Figure 2. Here, ReLU was used as the activation function for the real-valued model, and CReLU was used as the activation function for the complex-valued model. Typically, the complex-valued network produced a reconstruction closer to the ground truth, as evidenced by superior PSNR, NRMSE, and PSNR, than the real-valued network. Both networks typically outperformed CS with L_1-wavelet regularization.[3] Also, the complex-valued network produced a better phase reconstruction, as evidenced by superior NRMSE and PSNR compared to the real-valued network. In Supporting Information Figure S1, the red arrows suggest that the complex-valued network is able to better preserve and reconstruct phase details compared to the real-valued network.

3.2 | Experiment 2: Complex convolution and network width

The performance on a test dataset of the real and complex unrolled models as a function of network width is shown in Figure 3A. The number of iterations in each model was fixed at 4 as the number of feature maps was varied while keeping the total number of parameters for each model approximately the same. The reconstruction performance from networks with complex-valued convolutions had superior PSNR, NRMSE, and SSIM compared to the networks with real-valued convolutions. As expected, the performance of both networks improved as network width increased. The gap in performance between the real and complex models stayed fairly constant as the number of parameters increased. This figure is replotted over number of total feature maps instead of number of total parameters in Figure S2.

3.3 | Experiment 3: Complex convolution and network depth

Figure 3B shows similar trends to the results of experiment 2. Here, the number of feature maps is fixed as the number of iterations was varied while keeping the total number of parameters for each model approximately the same. The complex-valued model had superior PSNR, NRMSE, and SSIM compared to the real-valued model for all number of iterations. As expected, the performance of both networks improved as network depth increased.

3.4 | Experiment 4: U-Net performance

When complex convolution was used in the U-Net architecture, the reconstruction performance improved compared to the model with real convolution, with higher PSNR, lower NRMSE, and higher SSIM. The complex-valued CNN achieved superior PSNR (35.28 ± 2.34) compared to the real-valued CNN (35.00 ± 1.95). Additionally, the complex-valued CNN achieved superior NRMSE (0.16 ± 0.03) compared to the real-valued CNN (0.17 ± 0.02). However, the complex-valued CNN achieved approximately equal SSIM (0.90 ± 0.05) compared to the real-valued CNN (0.90 ± 0.02).

Representative images from the U-Net are displayed in Figure 4. Again, the complex-valued network produces a reconstruction closer to the ground truth than the real-valued network. The red arrows in Figure S3 indicate differences in the reconstruction of phase details between the various models and CS with L_1-wavelet regularization. These differences can be especially seen in the patellar tendon. As shown in the second column, the real-valued model introduced a phase wrapping error in the background of the phase images, whereas the complex-valued model and CS did not.

3.5 | Experiment 5: Dual gradient-echo dataset

In the unrolled network that was trained and tested on the dual-echo full-body dataset, the PSNR of reconstructions with complex-valued convolutions (29.51 ± 3.49) was superior to reconstructions with real-valued convolutions (28.54 ± 3.36). Additionally, the NRMSE of reconstructions with complex-valued convolutions (0.17 ± 0.02) was superior to reconstructions with real-valued convolutions (0.22 ± 0.08). Finally, the SSIM of reconstructions with complex-valued convolutions (0.78 ± 0.11) was superior to reconstructions with real-valued convolutions (0.77 ± 0.10).

Representative images from the unrolled network for the dual-echo full-body dataset are displayed in Figure 5. The model with complex-valued convolution often produced a much sharper reconstruction. Additionally, we observe from difference maps that the complex-valued model produced both a magnitude and phase reconstruction that was visually more similar to that of the reconstructed ground truth because the vessels and anatomical structure are more visible.

3.6 | Experiment 6: Fat-water separation

In the fat-water separation experiments on the dual-echo dataset, we calculated the pixel-wise percent error between the fat–water images of each model and the ground truth. On average, the fat–water separation of the complex model was 0.319% closer to the ground truth compared to the fat-water images of the real model. This pixel-wise percent error may be dominated by large errors in the fat–water separation. However, greater differences in performance can be seen in the actual fat–water images, as shown in Figure 6, which depicts fat and water maps of real, complex, and ground truth reconstructions for 2 different test patients. Red boxes highlight various discontinuations and inaccuracies in fat–water separation of the real model compared to the ground truth. The complex model was able to produce a more correct fat–water map for these regions. This suggests complex networks could be better for clinical applications involving fat–water separation.

3.7 | Experiment 7: Phase-contrast dataset

In the unrolled network that was trained and tested on the phase-contrast dataset, the PSNR of reconstructions with complex-valued convolutions (33.50 ± 5.90) was superior to reconstructions with real-valued convolutions (32.27 ± 5.54). Additionally, the NRMSE of reconstructions with complex-valued convolutions (0.21 ± 0.10) was superior to reconstructions with real-valued convolutions (0.22 ± 0.08). Finally, the SSIM of reconstructions with complex-valued convolutions (0.88 ± 0.08) was superior to reconstructions with real-valued convolutions (0.86 ± 0.08).

Representative images from the unrolled network for the phase-contrast dataset are displayed in Figure 7. In Figure 7A, magnitude images from the second echo only are shown. In Figure 7B, the velocity-encoded image is shown, which is calculated using both echoes. The model with complex-valued convolution consistently produced more accurate reconstructions, for which both the magnitude and velocity-encoded images were closer to the ground truth than the model with real-valued convolution and CS with L_1-wavelet regularization. This suggests that complex networks could be better for clinical cardiovascular applications.

3.8 | Experiment 8: Flow quantification

Results from the experiments comparing the real and complex models for flow quantification on the 2D PC data are shown in Figure 8, which compares the 2 models' performance, measured in percent error between the model and the ground truth, for 2 different flow metrics: average flow and peak velocity. The complex model had superior average flow estimation (6.27% error) than the real model (7.23% error). The peak velocity estimation of the complex model was 23.22% closer to the ground truth than that of the real model. Representative results are shown in Figure 9. From left to right in this figure are the real model reconstruction, complex model reconstruction, and ground truth reconstruction. This suggests that complex-valued networks may be more useful for the evaluation of blood flow of cardiac patients. Full-color videos are in the online-only Supporting Information Video S1.

4 | DISCUSSION

We have demonstrated that complex-valued CNNs can provide superior recovery of phase compared to purely real-valued, 2-channel CNNs, with clinical applications in fat–water separation and quantification of flow and velocity. We have also used complex-valued CNNs to significantly improve general MRI reconstruction compared to real-valued CNNs. In the majority of experiments, the complex-valued network achieved superior reconstructions compared to a real-valued network with the same number of trainable parameters.

Using complex networks to better reconstruct phase is a major novelty of this work. This can be best seen in the experiments done on phase-contrast MRI and associated flow quantification for cardiovascular applications, shown in Figure 9. Capture of peak velocities, which is critical to pressure gradient estimation, is markedly improved with complex networks. This is potentially because the complex network is better able to reconstruct each

temporal phase, thus creating more accurate velocity-encoded images and therefore more accurate estimations of average flow and peak velocity.

The significant impact of complex networks is also demonstrated on fat–water separation experiments, shown in Figure 6. There was not a large difference between complex and real networks in terms of pixel-wise percent error compared to the ground truth. However, this metric was calculated over the entire image and therefore does not necessarily accurately reflect the clinical impact of phase errors on interpretation of the images. A more clinically relevant assessment comes from inspecting the images to determine which networks had more areas where fat and water were erroneous swapped in the fat-water separated images. Figure 6 shows that the complex network is much more robust to difficult fat–water separation. Many areas are shown where the real network wrongly swapped fat and water, whereas the complex network did not. One possible explanation for this is the complex network can more accurately reconstruct phase than the real network.

Additionally, finer details in the phase are more visible in the complex-valued network, as shown by the red arrows in Figures 2B, 4B, and 5B. More accurate reconstruction of phase can especially be seen in the phase images of Figure 5B from the dual-echo body dataset and in the velocity-encoded images of Figure 7B from the phase-contrast dataset. In the dual-echo body dataset, accurate phase reconstruction was needed for correct fat–water separation. In the 2D PC dataset, accurate phase reconstruction was essential for quantifying flow in the velocity-encoded images.

Several reasons suggest that complex-valued networks could have superior performance compared to real-valued networks for MRI applications. First, maintaining phase information throughout the network is important because many MRI applications use the reconstructed phase as valuable information. The phase is decoupled in a 2-channel real and imaginary convolutional neural network because different weights are applied to both input channels, potentially altering the phase. Second, the complex-valued weights have been shown to contain higher representative power compared to real-valued weights. For example, complex numbers have been lauded for enabling faster training,[29] showing smaller generalization error[47] and even allowing the network to have richer representational power.[29,48]

The model with complex-valued convolution produced better image reconstructions over the model with real-valued convolution over a variety of architectures such as an unrolled network and a U-Net, as well as datasets such as a set of knee images, a set of dual-echo full-body images, and a set of phase-contrast images. We believe that there are 2 possible explanations for this. First, using complex-valued weights in our model with the complex-valued convolutional layer, we are able to use more feature maps so the number of parameters is the same as in the model with the real-valued convolutional layer; therefore, this enables better reconstruction accuracy.[8] Additionally, because the complex-valued network enforces a structure that preserves the phase of the input data, the reconstructed phase of the complex-valued network is typically visually closer (as measured by PSNR, NRMSE, and SSIM) to the phase of the ground truth compared to the reconstructed phase of the real-valued network.

When the width and depth of the unrolled network were varied over a large range, the complex-valued network still achieved superior image reconstruction metrics with a constant gap in performance compared to the real-valued model, even as the number of parameters greatly increased. Beyond quantitative metrics, the reconstructed images from the complex-valued network better show the details of anatomical structure. One possible explanation for this finding is that the complex-valued model can more accurately represent the complex-valued nature of the data compared to the real-valued model, which must learn this complex-valued nature. Therefore, the complex-valued model has an inherent advantage regardless of the network size. However, it is possible that we did not compare large enough models (due to GPU memory limitations) to see any potential convergence.

Across different complex-valued activation functions, CReLU achieved the best performance over the other, more complicated activation functions. These results suggest a potential for a better performing activation function for complex-valued networks; thus, future work could be directed toward exploring kernel activation functions, which allow the network to learn a trainable function for reconstructions, as described by Virtue et al[30] and Scardapane et al.[49]

DL approaches have some advantages compared to CS in terms of robustness, image quality, and reconstruction speed. Here, complex networks performed better than CS by quantitative metrics. It should be noted that in some examples the results of both the real and complex DL methods looked overly smoothed compared to the CS result. This phenomenon is most apparent in Figure 2. This is a known drawback of CNNs for image restoration, as shown by Zhao et al.[50] Despite this drawback, an advantage of these DL reconstructions over CS is greatly reduced reconstruction time. To address this drawback, we could use a better learning metric, such as a generative adversarial network, or add a perceptual loss to the reconstruction network.

Because we were using an off-the-shelf GPU with around 12 GB, we did have to constrain the number of layers and feature maps so our model would fit on this GPU. It is possible that our reconstruction performance would have been increased even further had we had access to a GPU with more memory. We could then have had more layers or feature maps—or even been able to treat our dataset as a volume instead of slices. This could also be easily extended to 4D datasets, where the time dimension could then be leveraged during the training of the model.

These methods are likely generalizable. Here, an unrolled network based on iterative soft-shrinkage algorithm and a U-Net were used as the 2 tested network architectures. We showed complex networks were better across both the unrolled and U-Net architectures, which suggests that the superior performance is generalizable across network architectures. The unrolled network that was used in this work has not been widely investigated, which is one aspect of the novelty of the work. However, this leaves open the question of the generalization of complex networks to network architectures other than unrolled and U-Net, which could be pursued as future work. This complex-valued framework can be easily adapted to any other network architecture by directly replacing the 2 channel real-valued convolution layers of existing networks with the complex convolution layers. Additionally,

the superior performance of complex-valued CNNs can be generalized to many other applications, both in MRI and otherwise. This has implications in other MRI applications where the reconstructed phase is important, such as in 4D flow and QSM. Outside of MRI, complex-valued networks could help DL tasks wherever complex numbers are used, such as ultrasound, optical imaging, radar,[51] speech,[21] and music.[21]

Possible future experiments include adding the complex conjugate of the filter matrix, $W = X - iY$, to the learned feature maps. This conjugate filter could potentially give the network more representative power without adding more trainable parameters. This could assist DL MRI applications where the physical phenomenon of the complex conjugate is encountered, such as in off-resonance correction. Additionally, complex-valued networks could be extended to quaternion-valued networks[52–54] with applications in DL-based reconstruction or RF pulse design.

5 | CONCLUSION

We have shown that complex-valued CNNs have superior image quality compared to real-valued CNNs on several tasks for which phase accuracy is clinically important, such as flow quantification and fat–water separation. Complex networks were able to more accurately quantify the flow in 2D PC datasets, which could lead to better clinical decisions for cardiac patients. Complex networks were also able to construct more continuous and accurate fat–water separated maps, which could lead to more accurate tasks further downstream, such as QSM or T_1 mapping. Additionally, we have explored a variety of complex-valued network architectures with superior results compared to real-valued architectures. Our work shows complex-valued CNNs provide superior reconstructions compared to real-valued CNNs with the same number of trainable parameters, enabling potentially reducing MRI scan times by more accurately reconstructing images from subsampled data acquisitions using complex-valued CNNs. Because of superior performance with deep complex-valued networks, we can improve the reconstruction of accelerated MRI scans. Complex-valued CNNs can be generalized to other reconstruction architectures and other DL MRI applications for which accurate phase reconstruction is important.

Supplementary Material

Refer to Web version on PubMed Central for supplementary material.

DATA AVAILABILITY STATEMENT

In the spirit of reproducible research, our formulation of complex-valued networks for MRI reconstruction can be found here: https://github.com/MRSRL/complex-networks-release.

REFERENCES

1. Griswold MA, Jakob PM, Heidemann RM, et al. Generalized autocalibrating partially parallel acquisitions (GRAPPA). Magn Reson Med. 2002;47:1202–1210. [PubMed: 12111967]

2. Pruessmann KP, Weiger M, Scheidegger MB, Boesiger P. SENSE: sensitivity encoding for fast MRI. Magn Reson Med. 1999;42:952–962. [PubMed: 10542355]

3. Lustig M, Donoho D, Pauly JM. Sparse MRI: the application of compressed sensing for rapid MR imaging. Magn Reson Med. 2007;58:1182–1195. [PubMed: 17969013]

4. Schlemper J, Caballero J, Hajnal JV, Price AN, Rueckert D. A deep cascade of convolutional neural networks for dynamic MR image reconstruction. IEEE Trans Med Imaging. 2018;37:491–503. [PubMed: 29035212]

5. Mardani M, Gong E, Cheng JY, et al. Deep generative adversarial neural networks for compressive sensing MRI. IEEE Trans Med Imaging. 2019;38:167–179. [PubMed: 30040634]

6. Yang G, Yu S, Dong H, et al. DAGAN: deep de-aliasing generative adversarial networks for fast compressed sensing MRI reconstruction. IEEE Trans Med Imaging. 2018;37:1310–1321. [PubMed: 29870361]

7. Diamond S, Sitzmann V, Heide F, Wetzstein G. Unrolled optimization with deep priors. 2017. arXiv:1705.08041 [cs.CV].

8. Cheng JY, Chen F, Alley MT, Pauly JM, Vasanawala SS. Highly scalable image reconstruction using deep neural networks with bandpass filtering. 2018. arXiv:1805.03300 [cs.CV].

9. Yang Y, Sun J, Li H, Xu Z. ADMM-net: a deep learning approach for compressive sensing MRI. 2017. arXiv:1705.06869 [cs.CV].

10. Hammernik K, Klatzer T, Kobler E, et al. Learning a variational network for reconstruction of accelerated MRI data. Magn Reson Med. 2018;79:3055–3071. [PubMed: 29115689]

11. Chen F, Taviani V, Malkiel I, et al. Variable-density single-shot fast spin-echo MRI with deep learning reconstruction by using variational networks. Radiology. 2018;289:366–373. [PubMed: 30040039]

12. Souza R, Lebel RM, Frayne R, Ca R. A hybrid, dual domain, cascade of convolutional neural networks for magnetic resonance image reconstruction. Proc Mach Learn Res. 2019;102:437–446.

13. Eo T, Jun Y, Kim T, Jang J, Lee HJ, Hwang D. KIKI-net: cross-domain convolutional neural networks for reconstructing undersampled magnetic resonance images. Magn Reson Med. 2018:80:2188–2201. [PubMed: 29624729]

14. Han Y, Yoo J, Kim HH, Shin HJ, Sung K, Ye JC. Deep learning with domain adaptation for accelerated projection-reconstruction MR. Magn Reson Med. 2018;80:1189–1205. [PubMed: 29399869]

15. Ronneberger O, Fischer P, Brox T. U-net: Convolutional networks for biomedical image segmentation. In: Lecture Notes in Computer Science (including subseries Lecture Notes in Artificial Intelligence and Lecture Notes in Bioinformatics). 2015.

16. Hyun CM, Kim HP, Lee SM, Lee S, Seo JK. Deep learning for undersampled MRI reconstruction. Phys Med Biol. 2018;63:135007. [PubMed: 29787383]

17. Lee D, Yoo J, Tak S, Ye JC. Deep residual learning for accelerated MRI using magnitude and phase networks. IEEE Trans Biomed Eng. 2018;65:1985–1995. [PubMed: 29993390]

18. Zhu B, Liu JZ, Cauley SF, Rosen BR, Rosen MS. Image reconstruction by domain-transform manifold learning. Nature. 2018;555:487–492. [PubMed: 29565357]

19. Cheng J, Wang H, Ying L, Liang D. Model learning: primal dual networks for fast MR imaging. In Proceedings of the International Conference on Medical Image Computing and Computer-Assisted Intervention (MICCAI 2019), Shenzhen, China. 2019. arXiv:1908.02426 [eess.IV].

20. Ke Z, Cheng J, Ying L, Zheng H, Zhu Y, Liang D. An unsupervised deep learning method for multi-coil cine MRI. Phys Med Biol. 2020;65:235041. [PubMed: 33263316]

21. Trabelsi C, Bilaniuk O, Zhang Y, et al. Deep complex networks. In Proceedings of the 6th International Conference on Learning Representations, (ICLR 2018), Conference Track Proceedings, Vancouver, British Columbia, Canada, 2018.

22. Dedmari MA, Conjeti S, Estrada S, Ehses P, Stocker T, Reuter M. Complex fully convolutional neural networks for MR image reconstruction. In Proceedings of First International Workshop, Machine Learning for Medical Image Reconstruction (MLMIR), at MICCAI 2018, Granada, Spain, 2018.

23. Wang S, Cheng H, Ying L, et al. DeepcomplexMRI: exploiting deep residual network for fast parallel MR imaging with complex convolution. Magn Reson Imaging. 2020;68:136–147. [PubMed: 32045635]

24. Wang S, Cheng H, Ke Z, et al. Complex-valued residual network learning for parallel MR imaging. In Proceedings of the 26th Annual Meeting of ISMRM, Paris, France, 2018. Abstract 2781.

25. El-Rewaidy H, Neisius U, Mancio J, et al. Deep complex convolutional network for fast reconstruction of 3D late gadolinium enhancement cardiac MRI. NMR Biomed. 2020;33:e4312. [PubMed: 32352197]

26. Tamir JI, Yu SX, Lustig M. Unsupervised deep basis pursuit: learning inverse problems without ground-truth data. In Proceedings of the 27th Annual Meeting of ISMRM, Montréal, Québec, Canada, 2019. Abstract 0660.

27. Liang D, Cheng J, Ke Z, Ying L. Deep magnetic resonance image reconstruction: inverse problems meet neural networks. IEEE Signal Process Mag. 2020;37:141–151. [PubMed: 33746470]

28. Sandino CM, Lai P, Vasanawala SS, Cheng JY. Accelerating cardiac cine MRI using a deep learning-based ESPIRiT reconstruction. Magn Reson Med. 2021;85:152–167. [PubMed: 32697891]

29. Arjovsky M, Shah A, Bengio Y. Unitary evolution recurrent neural networks. 2016. arXiv:1511.06464v4 [cs.LG].

30. Virtue P, Yu SX, Lustig M. Better than real: complex-valued neural nets for MRI fingerprinting. Accepted in Proceedings of the IEEE International Conference on Image Processing (ICIP), Beijing, China, 2017. arXiv: 1707.00070 [cs.CV].

31. Beck A, Teboulle M. A fast iterative shrinkage-thresholding algorithm for linear inverse problems. SIAM J Imaging Sci. 2009;2:183–202.

32. Sandino CM, Cheng JY, Chen F, Mardani M, Pauly JM, Vasanawala SS. Compressed sensing: from research to clinical practice with deep neural networks: shortening scan times for magnetic resonance imaging. IEEE Signal Process Mag. 2020;37:117–127.

33. Aggarwal HK, Mani MP, Jacob M. MoDL: model-based deep learning architecture for inverse problems. IEEE Trans Med Imaging. 2019;38:394–405. [PubMed: 30106719]

34. Souza R, Bento M, Nogovitsyn N, et al. Dual-domain cascade of U-nets for multi-channel magnetic resonance image reconstruction. Magn Reson Imaging. 2020;71:140–153. [PubMed: 32562744]

35. Hu Y, Xu Y, Tian Q, et al. RUN-UP: accelerated multishot diffusion-weighted MRI reconstruction using an unrolled network with U-Net as priors. Magn Reson Med. 2021;85:709–720. [PubMed: 32783339]

36. Seitzer M, Yang G, Schlemper J, et al. Adversarial and perceptual refinement for compressed sensing MRI reconstruction. 2018.

37. Ding PLK, Li Z, Zhou Y, Li B. Deep residual dense U-net for resolution enhancement in accelerated MRI acquisition. 2020. arXiv: 2001.04488 [eess.IV].

38. Kingma DP, Ba JL. Adam: a method for stochastic optimization. In Proceedings of the 3rd International Conference on Learning Representations, ICLR 2015, Conference Track Proceedings, San Diego, CA, 2015.

39. Wang Z, Bovik AC, Sheikh HR, et al. Image quality assessment: from error visibility to structural similarity. IEEE Trans Image Process. 2004;13:600–612. [PubMed: 15376593]

40. Epperson K, Sawyer AM, Lustig M, et al. Creation of fully sampled MR data repository for compressed sensing of the knee. In Proceedings of Society for MR Radiographers & Technologists (SMRT) 22nd Annual Meeting, Salt Lake City, UT, 2013.

41. Zhang T, Chen Y, Bao S, et al. Resolving phase ambiguity in dual-echo Dixon imaging using a projected power method. Magn Reson Med. 2017;77:2066–2076. [PubMed: 27221766]

42. Cheng JY, Zhang T, Ruangwattanapaisarn N, et al. Free-breathing pediatric MRI with nonrigid motion correction and acceleration. J Magn Reson Imaging. 2015;42:407–420. [PubMed: 25329325]

43. Uecker M, Lai P, Murphy MJ, et al. ESPIRiT—an eigenvalue approach to autocalibrating parallel MRI: where SENSE meets GRAPPA. Magn Reson Med. 2014;71:990–1001. [PubMed: 23649942]

44. Tamir JI, Ong F, Cheng JY, Uecker M, Lustig M. Generalized magnetic resonance image reconstruction using the Berkeley advanced reconstruction toolbox. In Proceedings of the ISMRM 2016 Data Sampling and Image Reconstruction Workshop, Sedona, AZ, 2016.

45. Lecun Y, Bengio Y, Hinton G. Deep learning. Nature. 2015;521:436–444. [PubMed: 26017442]

46. Berglund J, Ahlström H, Johansson L, Kullberg J. Two-point Dixon method with flexible echo times. Magn Reson Med. 2011;65:994–1004. [PubMed: 21413063]

47. Hirose A Complex-Valued Neural Networks: Advances and Applications. Vol 131. Berlin, Germany: Wiley-IEEE Press; 2011:2–8.

48. Wisdom S, Powers T, Hershey JR, Le Roux J, Atlas L. Full-capacity unitary recurrent neural networks. 2016. arXiv:1611.00035 [stat.ML].

49. Scardapane S, Van Vaerenbergh S, Totaro S, Uncini A. Kafnets: kernel-based non-parametric activation functions for neural networks. Neural Netw. 2019;110:19–32. [PubMed: 30481685]

50. Zhao H, Gallo O, Frosio I, Kautz J. Loss functions for image restoration with neural networks. IEEE Trans Comput Imaging. 2016;3:47–57.

51. Zhang Z, Wang H, Xu F, Jin YQ. Complex-valued convolutional neural network and its application in polarimetric SAR image classification. IEEE Trans Geosci Remote Sens. 2017;55:7177–7188.

52. Gaudet CJ, Maida AS. Deep quaternion networks. In Proceedings of the International Joint Conference on Neural Networks (IJCNN), Rio de Janeiro, Brazil, 2018.

53. Zhu X, Xu Y, Xu H, Chen C. Quaternion convolutional neural networks. 2018. arXiv:1903.00658.

54. Pavllo D, Grangier D, Auli M. QuaterNet: a quaternion-based recurrent model for human motion. In British Machine Vision Conference (BMVC), 2018, Newcastle, UK, 2018. arXiv:1805.06485 [cs.CV].
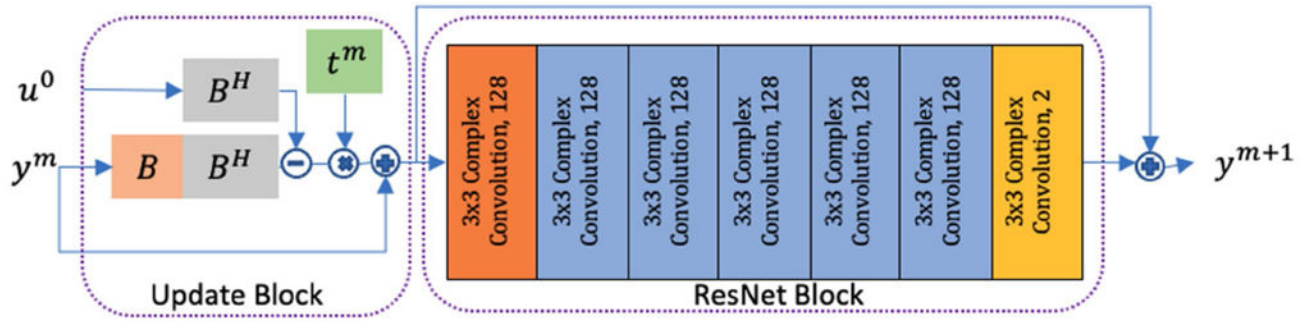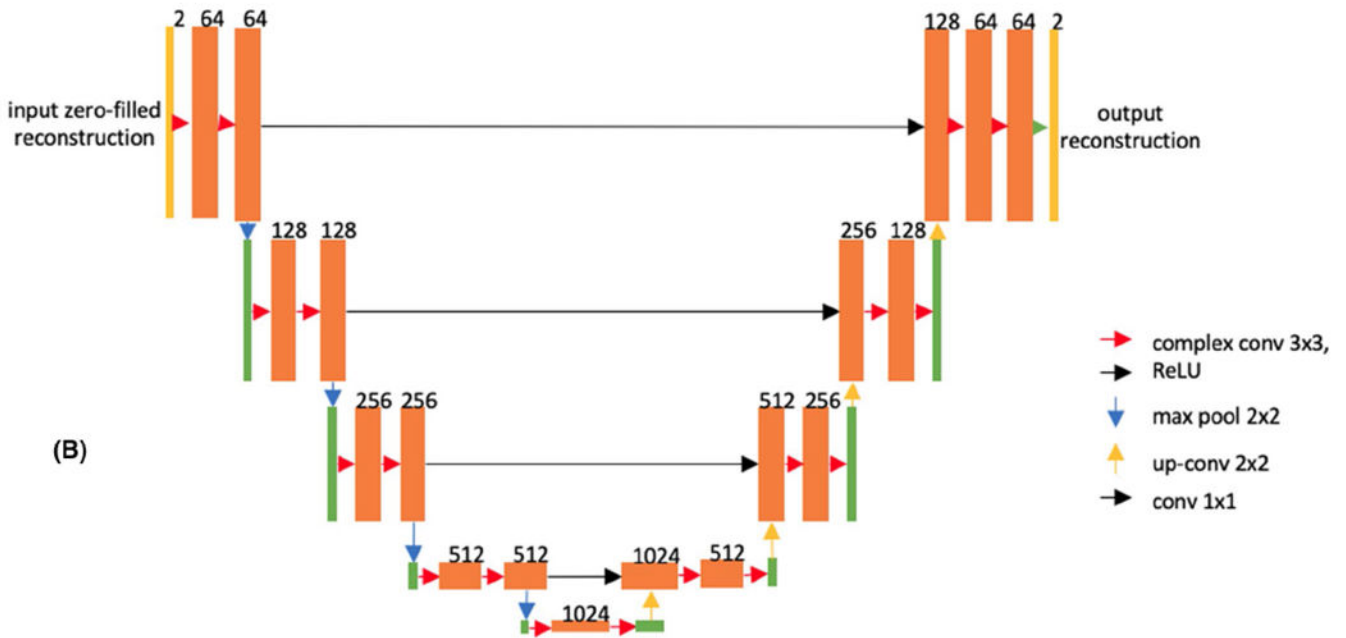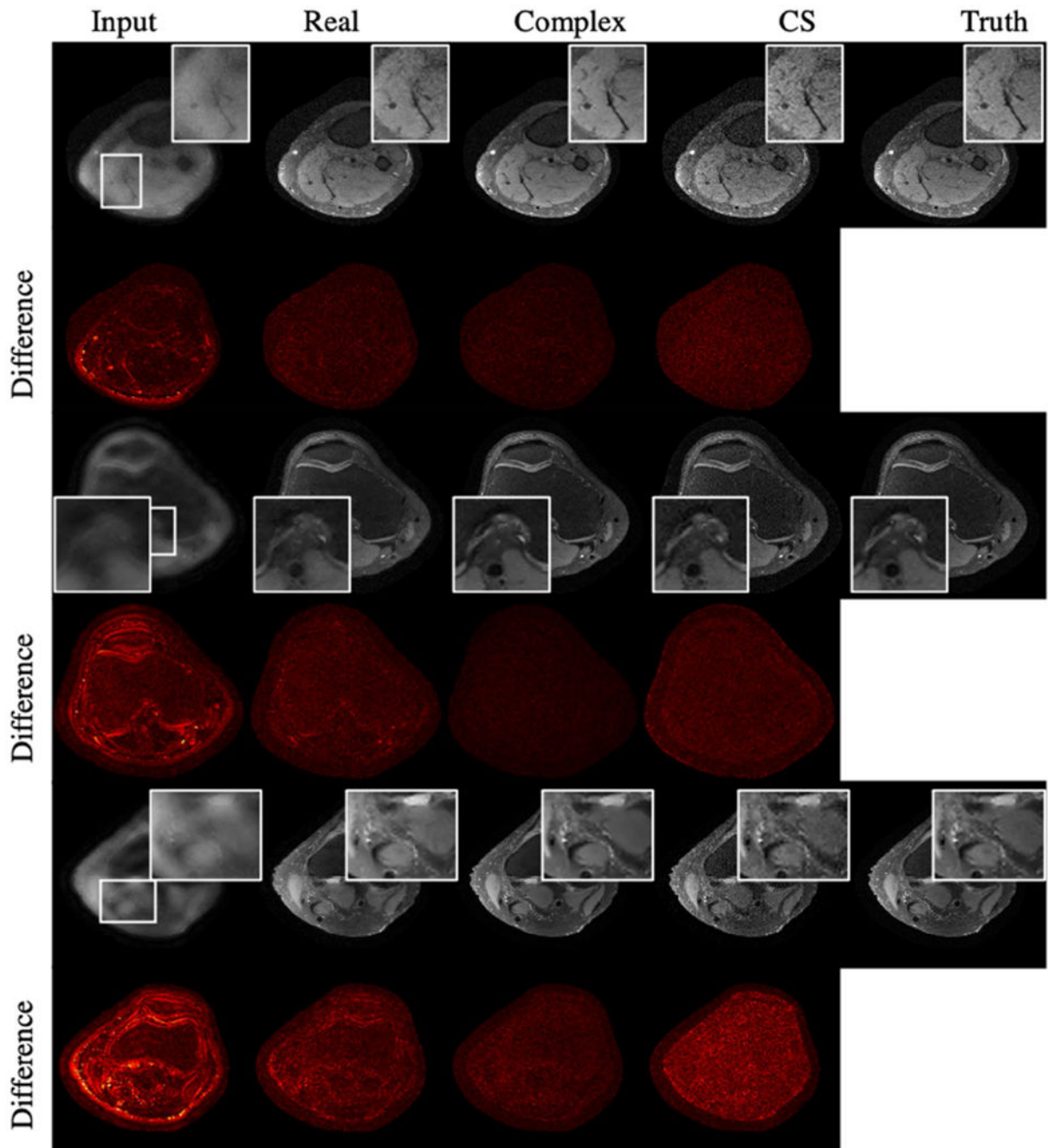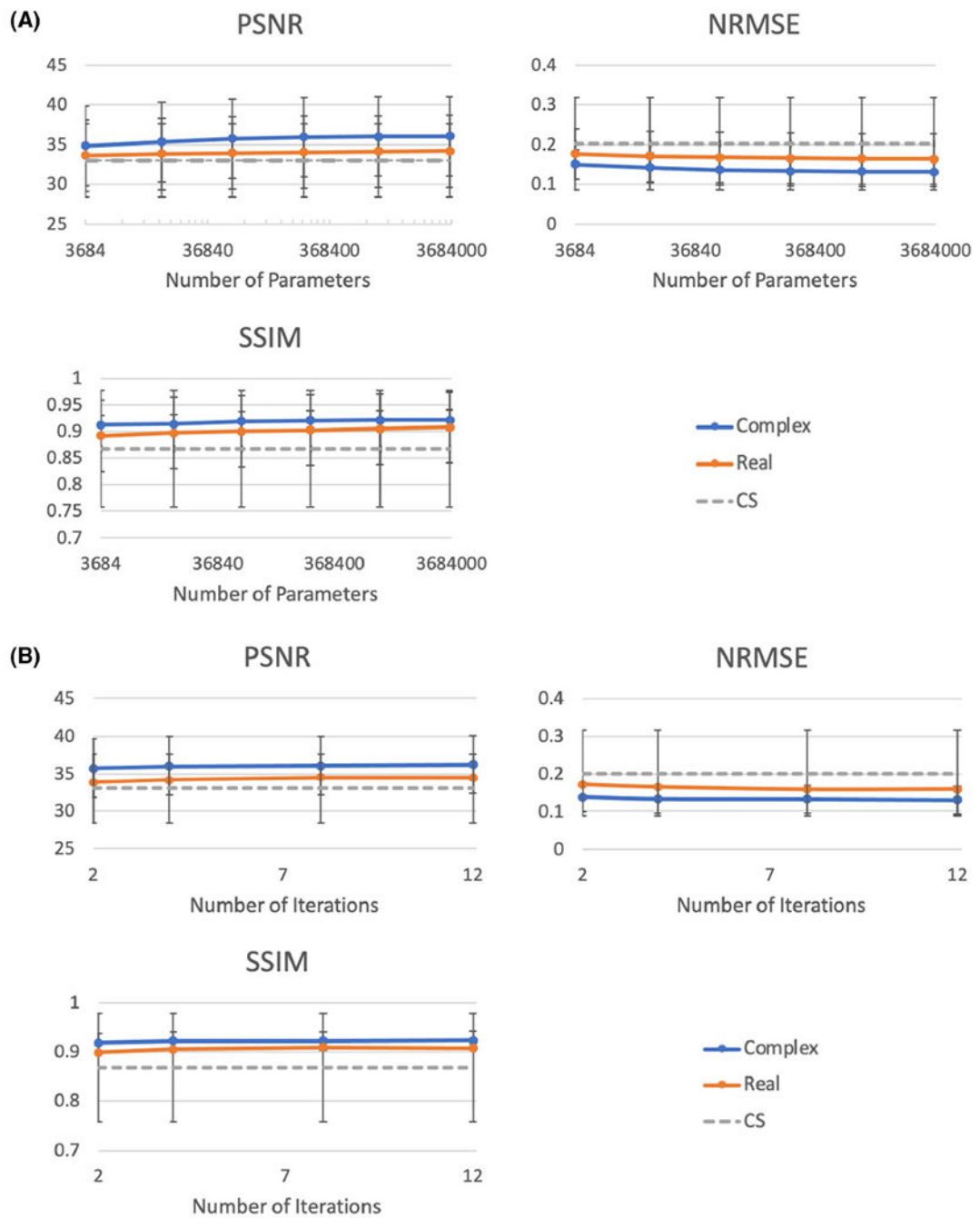
FIGURE 1.

A, One iteration of the unrolled network based on the iterative shrinkage-thresholding algorithm.[7,8] This consists of an update block, which uses the MRI model to enforce data consistency with the physically measured k-space samples. Then, a residual structure block is used to denoise the input image to produce the output image y^{m+1}. Each convolutional layer except for the last is followed by a ReLU and a complex-valued activation function (see Methods section B). B, The second reconstruction network architecture, which is based on the original U-Net for segmentation.[15] Every orange box depicts a multi-channel feature map. The number of channels is denoted on top of each feature map representation. Each arrow denotes a different operation, as depicted by the right-hand legend. This network uses contracting and expanding paths to capture information. *Note:* ReLU, rectified linear unit
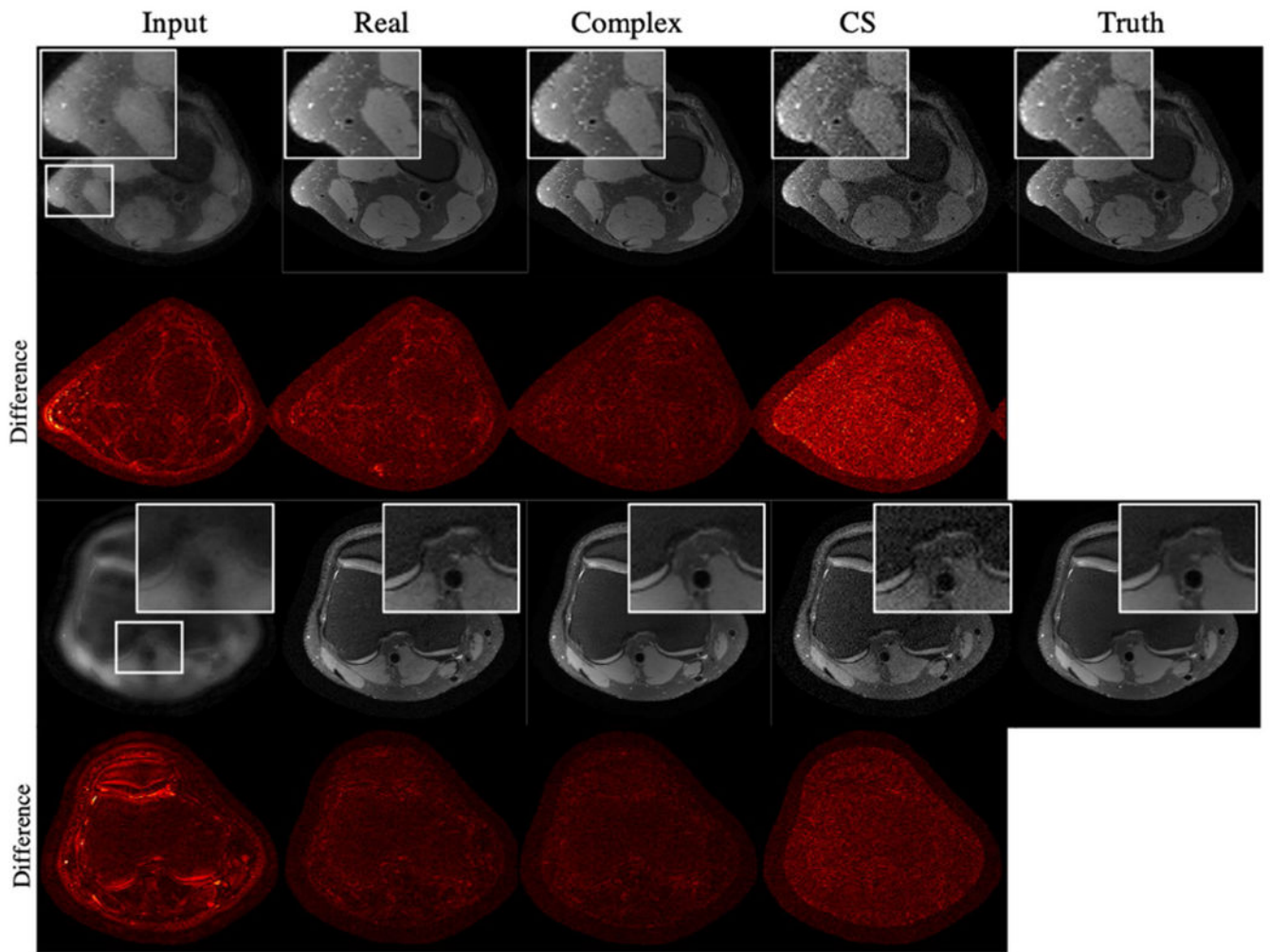
FIGURE 2.

Representative magnitude image results from the unrolled network, where the left column is the input zero-filled reconstructed image; the second column is the network with real convolution; the third column is the network with complex convolution; the fourth column is the compressed sensing with L_1-wavelet regularization reconstruction; and the fifth column is the ground truth reconstruction using all the data. Each row was undersampled by factors of 2.25, 7.40, and 7.37, from top to bottom. The difference maps are displayed under each reconstruction
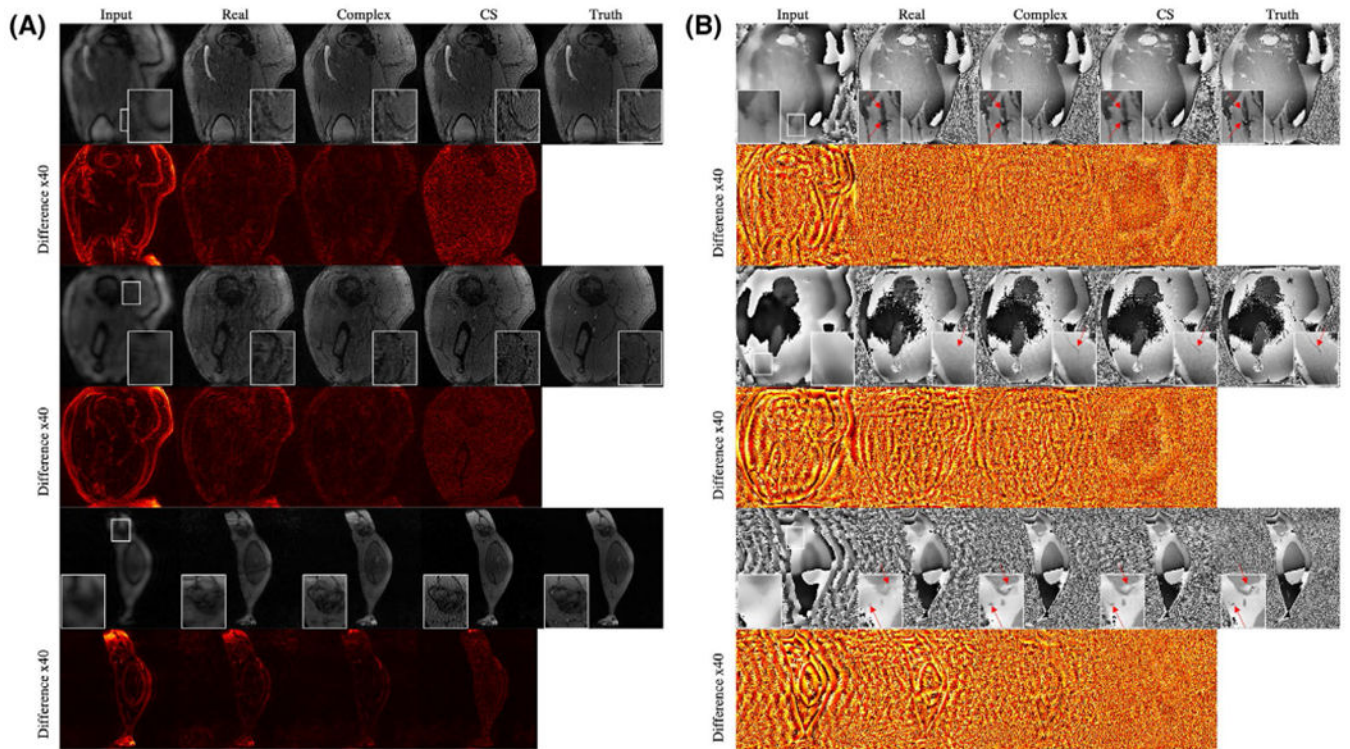
FIGURE 3.

A, Performance of the unrolled network as a function of network width on a test dataset. Here, the number of iterations is kept constant at 4, whereas the number of feature maps is varied for the complex and real networks such that the number of parameters for each evaluation is approximately the same. Compressed sensing does not use feature maps and is plotted as a constant. The test PSNR, NRMSE, and SSIM were evaluated for each network. B, Performance of the unrolled network as a function of network depth on a test dataset. Here, the number of feature maps is kept constant at 128 and 90 for the complex and real

networks, respectively, whereas the number of iterations is varied for each network. The number of iterations in compressed sensing does not change; however, its performance is plotted for reference. The test PSNR, NRMSE, and SSIM were evaluated for each network. *Note:* NRMSE, normalized RMS error; PSNR, peak SNR; SSIM, structural similarity index
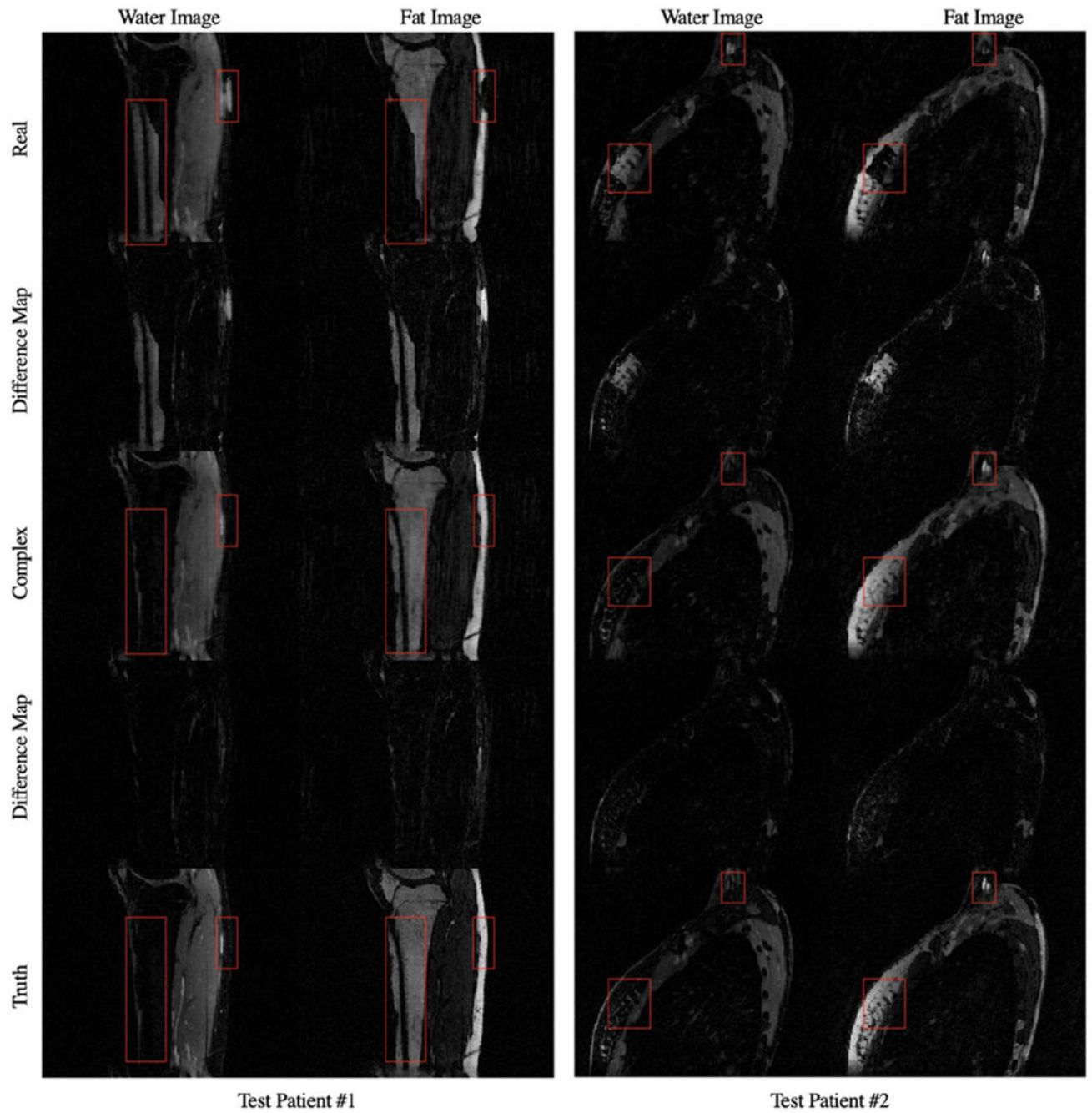
FIGURE 4.
Representative magnitude image results from the U-Net, where the left column is the input zero-filled reconstructed image; the second column is the network with real convolution; the third column is the network with complex convolution; the fourth column is the compressed sensing with L_1-wavelet regularization reconstruction; and the fifth column is the ground truth reconstruction. The top row was undersampled by a factor of 4, and the bottom row was undersampled by a factor of 6. The difference maps are displayed under each reconstruction
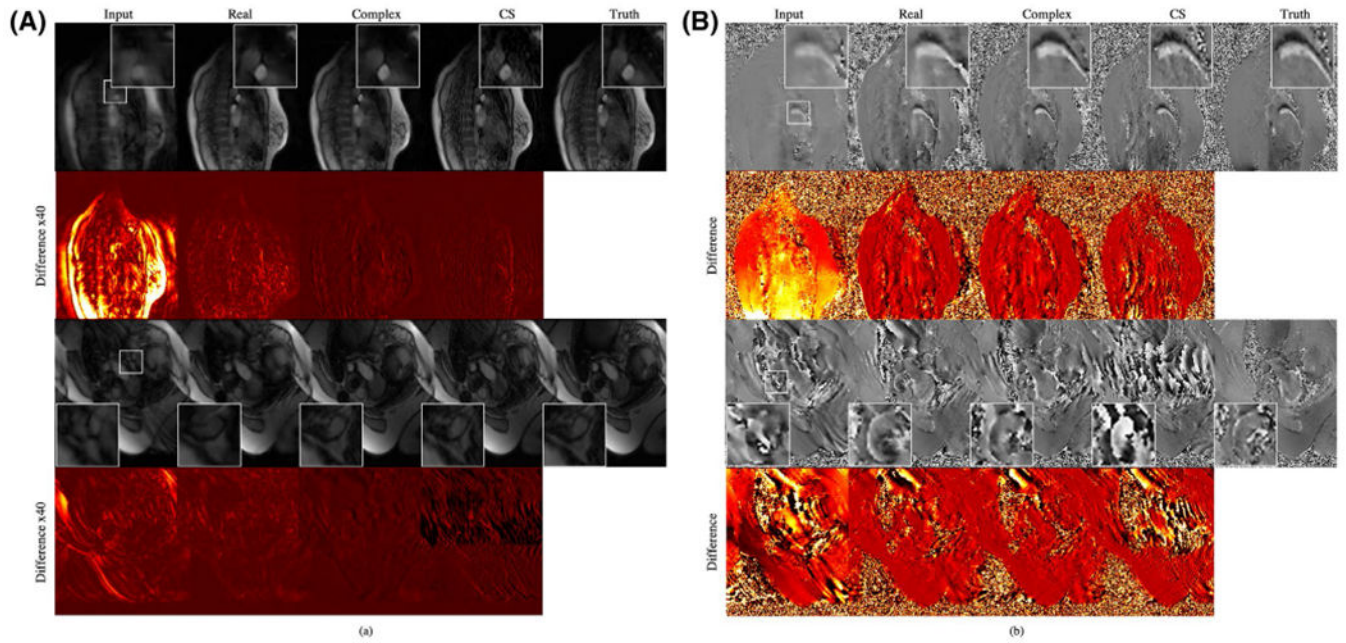
FIGURE 5.

Representative results from the unrolled network from the dual gradient-echo dataset, where the left column is the input zero-filled reconstructed image; the second column is the network with real convolution; the third column is the network with complex convolution; the fourth column is the compressed sensing with L_1-wavelet regularization reconstruction; and the fifth column is the ground truth reconstruction. Each row was undersampled by factors of 6, 9, and 4, from top to bottom. The difference maps, magnified by a factor of 40, are displayed under each reconstruction. A, Magnitude images. B, Phase images. Red arrows indicate differences in visibility of small details
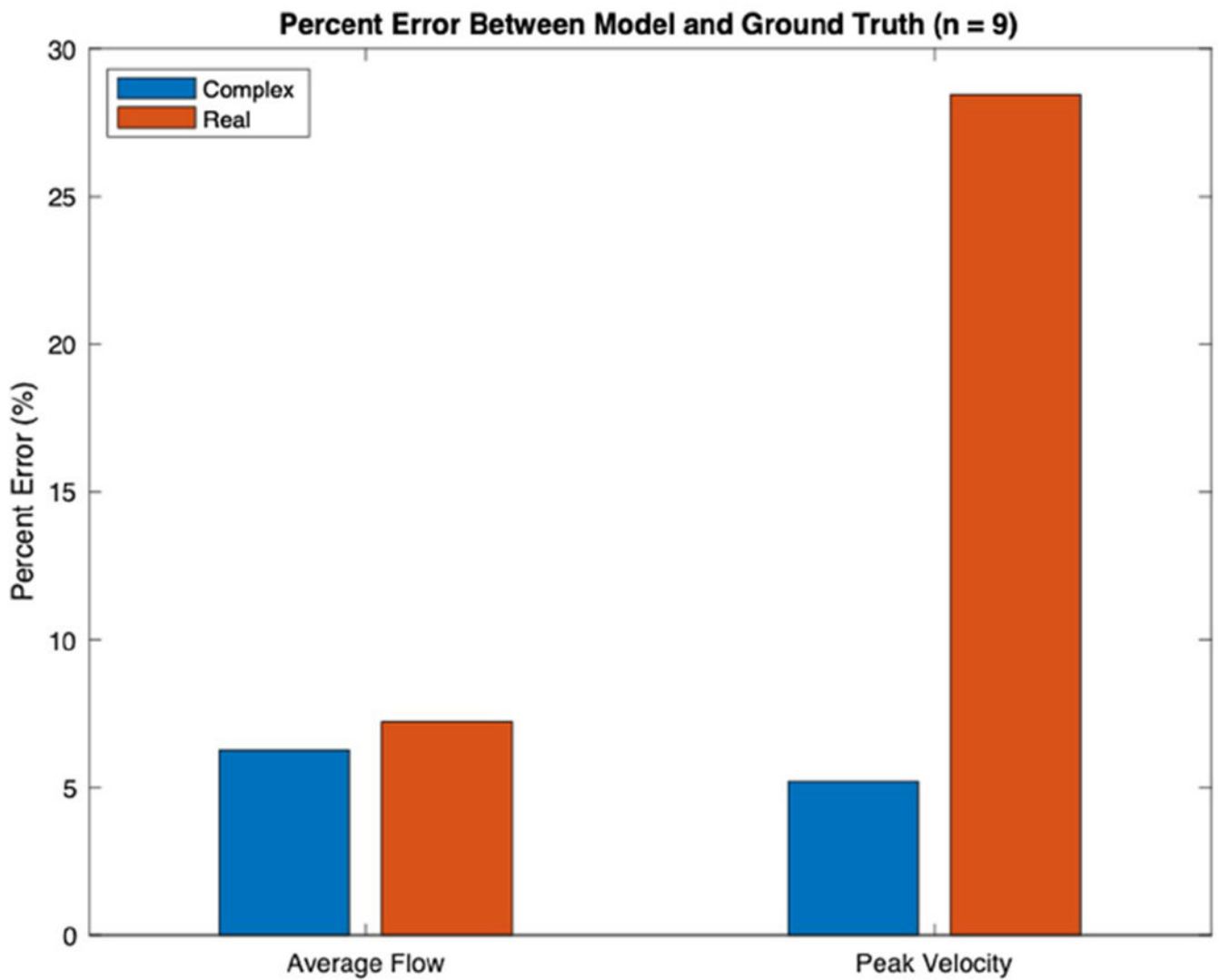
FIGURE 6.

The fat and water maps of the real, complex, and ground truth reconstructions for 2 different test patients. The red boxes highlight various discontinuations and inaccuracies in the fat–water separation of the real model compared to the ground truth. The complex model was able to produce a more correct fat–water map for these regions
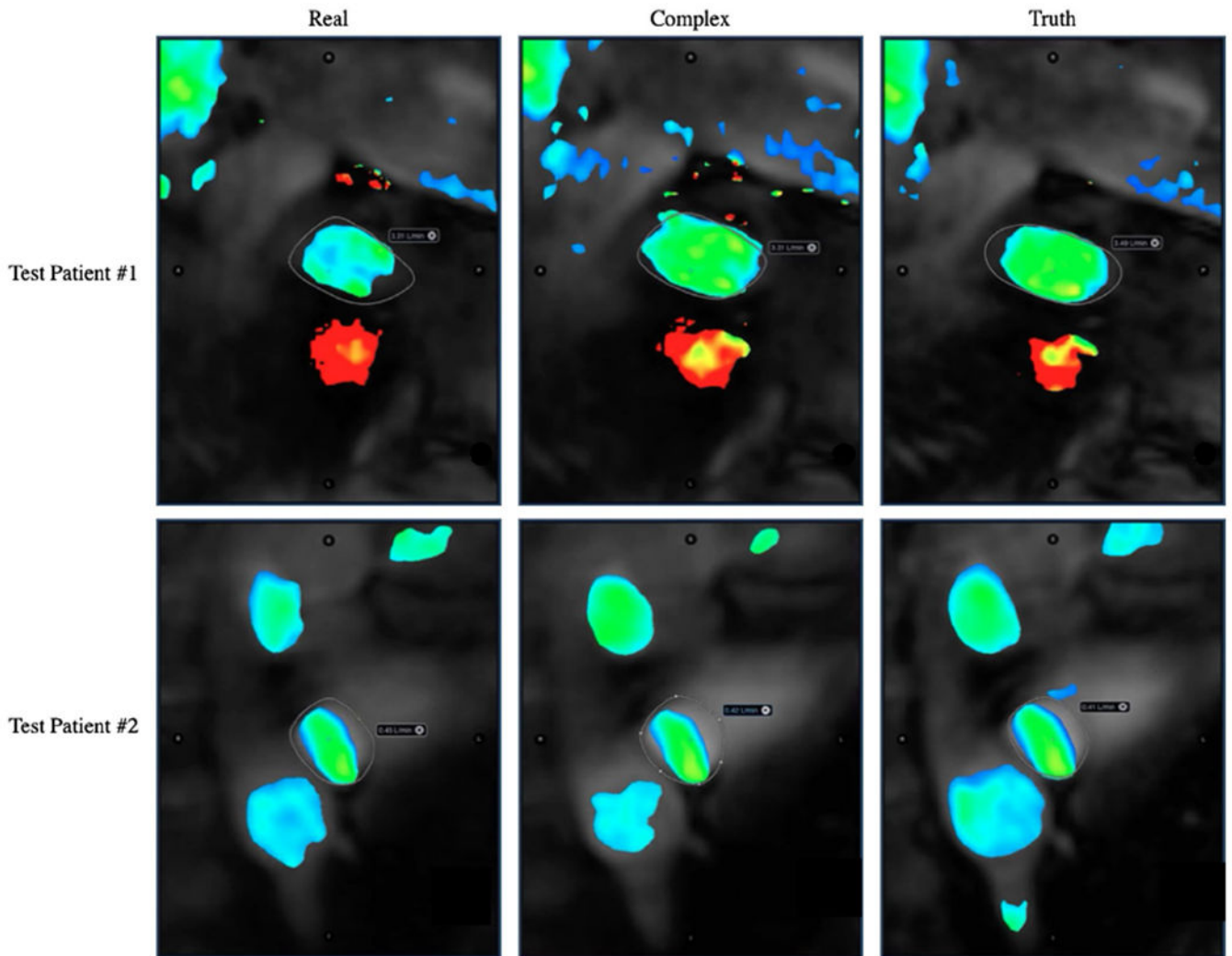
FIGURE 7.

Representative results from the unrolled network of the phase-contrast dataset, where the left column is the input zero-filled reconstructed image; the second column is the network with real convolution; the third column is the network with complex convolution; the fourth column is the compressed sensing with L_1-wavelet regularization reconstruction; and the fifth column is the ground truth reconstruction. Each row was undersampled by factors of 9, 6, and 4, from top to bottom. The difference maps are displayed under each reconstruction. A, Magnitude images of the second echo. B, Velocity-encoded images

FIGURE 8.

Quantitative results from the experiments comparing the real and complex models for flow quantification on the 2D PC dataset. This plot compares the 2 models' performance, measured in percent error between the model and the ground truth, for 2 different flow metrics: average flow and peak velocity. The complex model had superior average flow estimation (6.27% error) than the real model (7.23% error). The peak velocity estimation of the complex model was 23.22% closer to the ground truth than that of the real model

FIGURE 9.

Visual results from the experiments comparing the real and complex models for flow quantification on an exam from the 2D PC dataset. From left to right are the reconstruction of the real mode, reconstruction of the complex model, and reconstruction of the ground truth. For test patient 1, the average flow estimation across all phases is 3.31 L/min, 3.31 L/min, and 3.49 L/min; and the peak velocity estimation is 270.82 cm/s, 124.59 cm/s, and 107.63 cm/s, for the real, complex, and ground truth, respectively. For test patient 2, the average flow estimation across all phases is 0.45 L/min, 0.42 L/min, and 0.41 L/min; and the peak velocity estimation is 106.63 cm/s, 99.2 cm/s, and 96.31 cm/s, for the real, complex, and ground truth, respectively. Full color videos are in the online-only Supporting Information Video S1

TABLE 1

Comparison of image metrics on test knee datasets with various complex-valued activation functions. The bold values denote which model performed the best under each image metric. Variable-density subsampling (R = 7.9 ± 0.1)

Method	NRMSE	PSNR	SSIM
Input images	0.72 ± 0.10	24.73 ± 2.4	0.76 ± 0.08
Real convolution with ReLU	0.39 ± 0.09	30.47 ± 2.5	0.88 ± 0.07
Complex convolution with:			
CReLU	$\mathbf{0.31 \pm 0.08}$	$\mathbf{32.32 \pm 3.6}$	$\mathbf{0.90 \pm 0.06}$
modReLU	0.38 ± 0.09	30.67 ± 3.5	0.87 ± 0.07
zReLU	0.32 ± 0.09	31.97 ± 3.4	0.89 ± 0.06
ReLU	0.33 ± 0.08	31.88 ± 3.4	0.89 ± 0.07
Cardioid	0.32 ± 0.09	31.86 ± 3.4	0.89 ± 0.06

Abbreviations: NRMSE, normalized RMS error; PSNR, peak SNR; ReLU, rectified linear unit; SSIM, structural similarity index.